Load–Displacement Behavior of Helical Shape Memory Alloy Spring Actuators with Small Spring Diameter to Wire Diameter Ratios

Ryan Puchaty[1] · Giovanni De Vita[1] · Raj Vaidyanathan[1]

Abstract A design methodology for fabricating and predicting the load–displacement behavior of shape memory alloy (SMA) spring actuators has been previously created and validated (Nicholson et al., Smart Mater Struct 23(12):13–23, 2014). However, it was found in this work that for springs with a spring index (ratio of spring diameter to wire diameter) below five, the load–displacement response of shape memory spring actuators no longer fits the previously established model. This paper explores the use of a correction factor in the governing equations to account for the plastic deformation that occurs when fabricating springs with very small spring indices. The plastic deformation induces an effective reduction in the volume of the transforming material, thus reducing the load-bearing and actuation capabilities of the spring. A semi-analytical solution to this problem is found which can be used to predict the load–displacement behavior. This is accomplished through a reduction in the effective wire diameter based on the approximate shear strain during loading. This approach is consistent with observations during thermo-mechanical cycling in SMAs, where the phase transformation remained mostly unhindered despite large residual inelastic and/or plastic strains, and has direct application in

the design of actuators with small spring indices by quantifying the drop in actuation force and stroke.

Keywords Shape memory spring · Transformation strain · Load–displacement

✉ Raj Vaidyanathan
raj@ucf.edu

1 Advanced Materials Processing and Analysis Center, Materials Science and Engineering, Mechanical and Aerospace Engineering, University of Central Florida, 4000 Central Florida Blvd., Orlando, FL 32816, USA

Introduction

Shape memory alloys (SMAs) have been widely used as actuators due to their ability to recover high strains (up to 8%) elastically. Their high work density of 10 J/cm^3 is nearly double that of hydraulic-based actuation systems and makes them ideal for several applications, particularly in the aerospace, automotive, and medical industries where space and weight are of critical concern [2]. Most applications of SMA actuators are linear; however, current efforts in SMA development are moving toward multi-axial applications. Boeing's reconfigurable rotor blade technology uses SMA torque tubes to twist propeller blades and improve efficiency [3], while NASA is using similar technology to change the geometry of aircraft wings [4, 5]. SMA-based bimetallic strip smart actuators have been designed which can achieve the necessary forces for adaptive structures in space applications [6]. NASA Glenn Research Center has shown that shape memory springs show potential in CubeSats where space is at a premium [7].

SMA springs have also been widely used as actuators that experience multi-axial loading. Springs are a popular choice as energy-storing mechanisms due to their engineering versatility coupled with their ease of manufacture. They can be implemented in a wide variety of configurations and can achieve large strokes or forces, as required. More importantly, the behavior of linear springs is well

understood and can be correctly predicted, making them ideal for applications where reliability is a key parameter. Some of the key limitations of springs (such as their tendency for unwanted buckling and instability) can be fixed by designing the ends of the springs with certain characteristics. While plain ended springs are the easiest to make, they have disadvantages compared to ground or squared springs, which offer improved stability and ensure proper contact with the integrating structure [8, 9]. The principal challenge in working with SMA springs is accurately modeling their behavior. While SMAs are anisotropic and do not exhibit a linear stress/strain relationship, under certain configurations, SMA springs can be modeled with an apparent isotropic modulus to accurately predict their behavior [1] based on known spring mechanics [10]. As devices get smaller and the force requirements for these actuators increase, studying and predicting the behavior of SMA springs with non-traditional (e.g., small) spring indices (ratio of spring diameter to wire diameter) become ever more important as their behavior can no longer be easily predicted. This oftentimes results in these smaller springs not producing the requisite actuation force and associated stroke. Without an accurate model to predict this force, the designer has to rely upon empirical iterative fabrication and testing steps that lead to unnecessary costs. This paper acquires data from springs with a range of spring indices and examines the applicability of the previously accepted methodology in modeling the data. It identifies a range of spring indices for which the previous established methodology [1] is applicable. For the range in which it is not, it justifies and introduces a correction factor that considers the plastic deformation resulting from the fabrication process typically employed to make small springs. This modification is accomplished by considering both the mechanics of helical springs and aspects of SMA behavior. The end result is an accurate way of predicting the actuation force and stroke for a shape memory helical spring actuator over the range of useful spring indices that can be incorporated in engineering applications.

Experimental Procedures

The springs tested in this work were fabricated from as-drawn, commercially available, NiTi wire (nominal composition 54.5 wt% Ni and 45.5 at.% Ti) with a nominal wire diameter, d, of 1.5 mm. The starting martensite start, M_s, martensite finish, M_f, austenite start, A_s, and austenite finish, A_f temperatures were 9, −13, 51, and 61 °C, respectively. The springs were formed in multiple steps using up to seven steel mandrels with progressively decreasing mean spring diameters, D, to produce the final shape. At each step, the wire was wound onto a steel

mandrel and constrained with a sleeve and shape set at 525 °C for 30 min in air and subsequently furnace-cooled to room temperature prior to removing the sleeve. This process was repeated until the desired geometry was achieved. The final geometries for the springs used in these experiments are listed in Table 1 with the corresponding geometrical parameters shown in Fig. 1. The design of all springs employed in these experiments was plain-ground ends as shown in Fig. 1. Plain-ground ends facilitated ease of removal from the mandrel and good electrical contact during Joule heating. Spring outer and wire diameters were measured and averaged across several points to report the mean spring diameters and spring indices, C or $\frac{D}{d}$, reported in Table 1. The spring pitch, P, was determined from the mandrel geometry.

The spring load–deflection data following heating above the austenite finish temperature were obtained by modifying the test setup developed in [1] and are shown in Fig. 2a. The setup was originally capable of testing springs in tension with a maximum load of 22 N and was modified in this work to facilitate testing in compression with a maximum load of 444 N. To accommodate the greater loads and facilitate data acquisition while redirecting the load, additional pieces were designed and implemented. The applied load is transferred into a linear thrust bearing maintaining rotational independence and operating under safe load limits of the torque cell and angular position sensor. As shown in Fig. 2a, two 9.525 mm diameter precision guide rods were added with the 8 mm spline rod. This increased the rotational stability of the fixture perpendicular to the testbed and maintained linear concentricity and independence. As shown in Fig. 2b, guide pin pairs were used for buckling compensation to combat the effects of the plain ends and small spring indices. The pins act as a restoring force on the springs under compressive

Table 1 Parameters of the experimental springs

	d(mm)	D(mm)	C	α(°)	N_a
Spring 1	1.5	8.1	5.41	9.50	3
Spring 2	1.5	7.5	4.98	12.00	4
Spring 3	1.5	6.7	4.47	11.44	5
Spring 4	1.5	6.1	4.04	10.83	4
Spring 5	1.5	5.5	3.73	11.91	5
Spring 6	1.5	5.1	3.38	12.66	4
Spring 7	1.5	4.1	2.73	12.00	4

The columns represent the data from left to right; the wire diameter, d; the spring mean diameter, D; the spring index, C or $\frac{D}{d}$; the helical angle, α; and the number of active coils, N_a. Figure 1 illustrates the relevant parameters
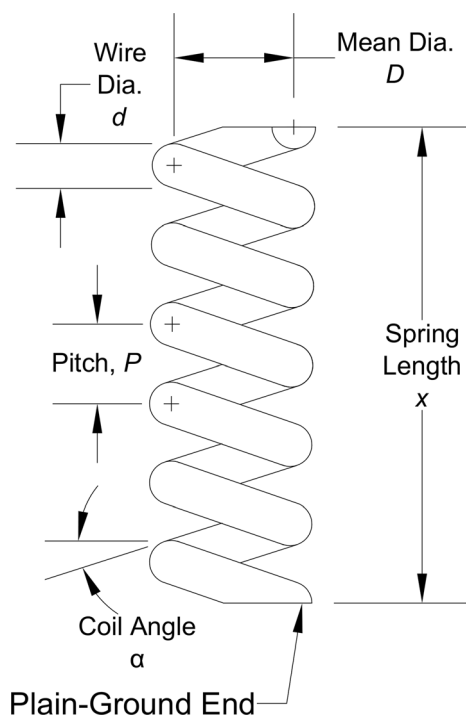
Fig. 1 Geometric parameters of helical springs tested and are listed in Table 1 for the various springs tested
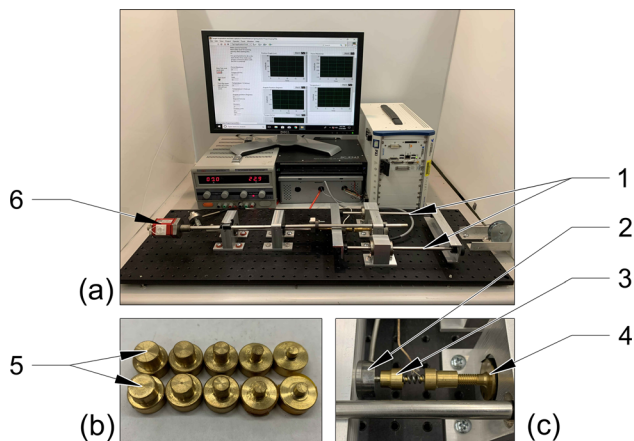

Fig. 2 Modified setup from [1] for characterizing shape memory alloy spring actuators in compression: **a** fully instrumented testing set up with a LabVIEW interface for data acquisition. Two 9.525 mm precision guide rods (1) and pins (3) used for buckling compensation, **b** close up view of guide pin pairs (5) used to mitigate buckling and **c** close up of test spring fixture. The applied force from the pulley is recorded with the load cell (2) and transferred to the thrust bearing (4). The stroke is recorded through a magnetostrictive position sensor (6)

test loads. An OMEGA LC202-100 load cell was added in line with the springs, as shown in Fig. 2c.

Actuation of the springs was accomplished through forced convection (for spring indices below 4.1) and Joule heating (for spring indices above 4.1). Heat transfer from the spring ends caused unacceptable temperature gradients

in the springs with low spring indices during Joule heating. Forced convection heating proved an effective mode of heat transfer for actuation for these indices. The wire temperature was monitored with a K-type thermocouple. The targeted wire temperature was 150 °C, well above the 61 °C austenite finish temperature to compensate for any changes arising from evolutionary behavior. This allowed for repeatable actuation and a ± 15 °C tolerance during the tests as well as ensuring there were no residual effects from retained martensite [11].

Results and Discussion

Figure 3a–g shows the acquired data as symbols in the applied load vs displacement or contraction graphs. The lines through the data follow the methodology adopted in [1] to model the acquired data. A summary of the methodology from [1] is given in the following. An iterative process that accounted for the evolving geometry of the spring was developed to accurately predict SMA spring displacement using the following equations. The shear modulus, G, used for calculation was $25 GPa$, and the Poisson ratio was 0.413.

$$\delta = \frac{8FD^3 N_a}{Gd^4}\left(1 - \frac{3}{16C^2} + \frac{3+v}{2(1+v)}\tan^2(\alpha)\right), \qquad (1)$$

$$\alpha = \tan^{-1}\left(\frac{P}{\pi D}\right), \qquad (2)$$

$$L = \frac{N_a \pi D_0}{\cos(\alpha_0)}, \qquad (3)$$

$$D = \frac{L\cos(\alpha)}{N_a \pi}, \qquad (4)$$

$$x = N_a P_0 - \delta, \qquad (5)$$

$$P = \frac{x}{N_a}, \qquad (6)$$

$$x_0 = N_a P_0, \qquad (7)$$

$$C = \frac{D}{d}, \qquad (8)$$

where the displacement or contraction, δ, in Eq. 1, is related to the load, F, as a function of SMA properties, namely, the shear modulus, G, and the Poisson's ratio, v, as well as the spring and wire geometry, namely, the wire diameter, d, the mean spring diameter, D, the helix angle, α, the spring index, C, and the total number of turns in the spring, N_a. Combining Eq. 1 with an iterative process that recalculates the spring geometry as it is loaded using Eqs. 2–8 further improves the accuracy of the displacement prediction, especially for large strokes. These equations account for the varying geometry as the spring changes

Fig. 3 Acquired load–displacement data of shape memory alloy spring actuators with decreasing spring indices, C (ratios of spring diameter to wire diameter). Symbols are the experimental load–displacement data and the lines are generated from Eqs. 1 to 8 following [1]
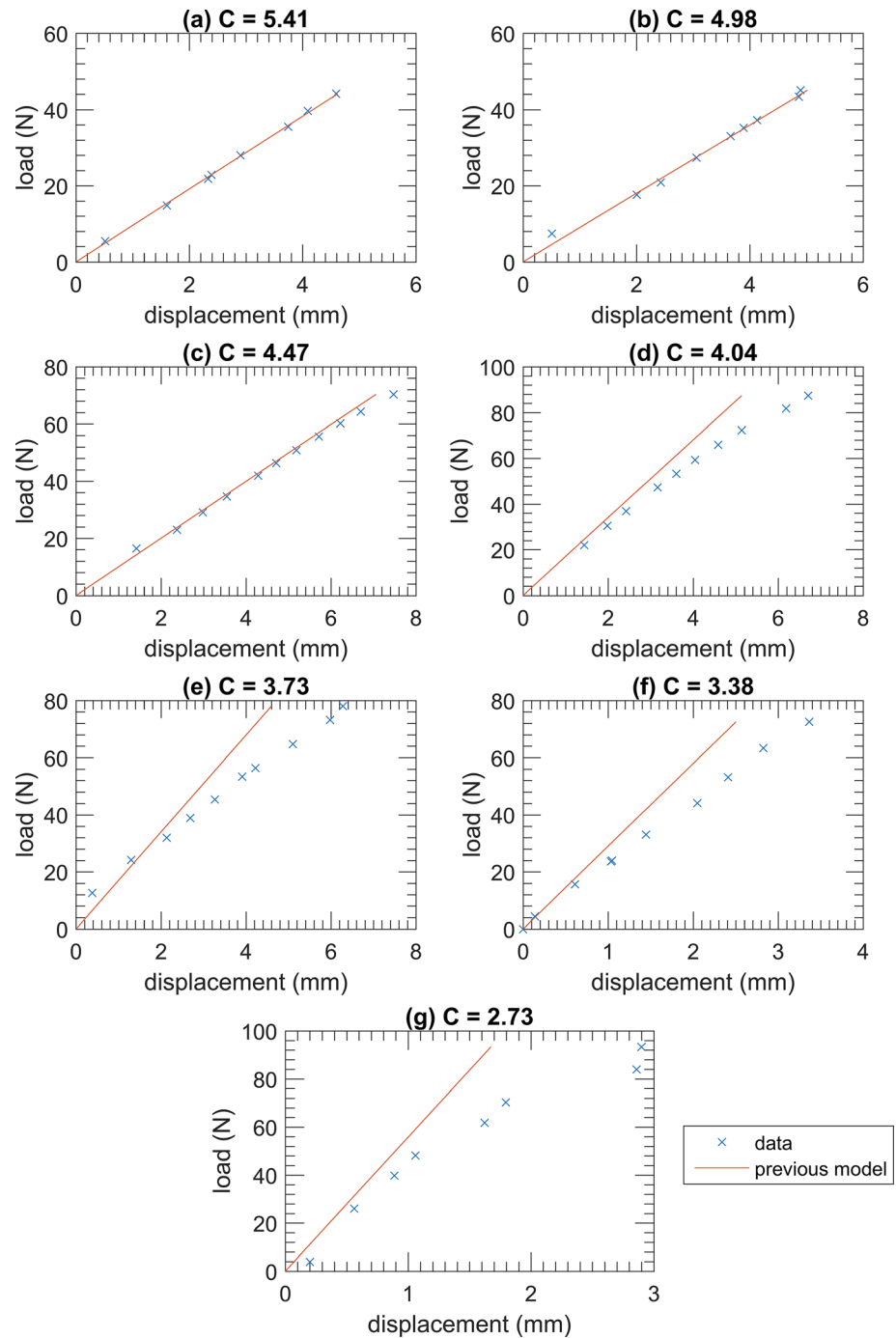
length. The pitch, P, is a function of the spring free length, x. The new diameter is determined at each iteration from the constant wire length, L, where D_0, P_0, x_0, and α_0 are the initial spring diameter, pitch, spring length, and helix angle, respectively. The aforementioned methodology matches the data for compression springs reasonably well as seen in Fig. 3a–c. However, the model began to deviate at spring indices below 5, which can be seen in Fig. 3c–g. The deviation is more marked at lower spring indices (close to 4 and below). To effectively implement these

springs as actuators in various designs, a model for predicting the behavior at the first cycle and thereafter in subsequent cycles is needed. Of particular importance is to predict the first cycle behavior of the springs that often exhibit the highest loadings and extensions [12].

To account for this deviation, the method of fabricating the spring is considered. As outlined in the experimental procedures section, the springs were manufactured using shape setting in multiple steps, with each subsequent shape set resulting in a smaller mean diameter, to achieve the

desired geometry. This process introduces permanent plastic strain along the innermost and outermost radius of the spring similar to an overloaded torsion spring. The strain is not fully removed between shape sets as the springs are shape set at 525 °C and not annealed, leaving a residual plastic strain at the inner and outer diameters of the spring. For large spring indices, this would have a small effect on the total strain in the wire under load. As the permanent strain increases from further mean spring diametral reduction, the effects become apparent at all loadings. This manifests as a deviation from model behavior in Fig. 3c–g.

To account for this phenomenon of increasing plastic strain, a continuously decreasing effective wire diameter, d_{eff}, with increasing load was implemented. The wire diameter is decreased every iteration using a loss factor, κ. This factor follows the compounded loss of material due to the shear strain, $\epsilon_{\mathrm{r}\theta}$, and is incorporated in the previously established methodology [1] in Eqs. 1–8. The shear strain in the spring results from axial loading of the spring and the normal strain from the bending moment during the manufacture of the springs. As the loading increases, an area starting from the outside diameter of the wire is initially strained. This process is analogous to a rod subject to torsional loading, where linearly increasing strain starts at zero at the center of the wire diameter and increases to a maximum at the outer wire radius. This affects the previously strained region from the bending of the wire along the spring axis. As this region is additionally stressed, it plastically deforms and no longer provides the same stress from the phase transformation leading to an effective reduction in the contributing area. The area of interaction is not expected to be circular, but for practical reasons, this is represented as a continuously decreasing diameter. This approach is also consistent with previously observed behavior in SMAs where plastic deformation due to, e.g., cycling does not affect the phase transformation characteristics (in strain space) and merely reduced the volume of the effective transforming material [12–15].

Thus, the effective wire diameter, d_{eff}, takes the form of Eq. 9, resulting in a revised effective spring index, C_{eff}. In Eq. 9, an interval, n, is arbitrarily chosen to ensure that the interval or loading steps in which d_{eff} is determined is adequate and meets a convergent minimum in the discretized implementation. This also allows for more granularity of the loss factor than if the model adopted a non-iterative approach.

$$d_{\mathrm{eff}} = d_0 \left(1 - \frac{\kappa}{n}\right)^{n\epsilon_{\mathrm{r}\theta}}, \tag{9}$$

$$C_{\mathrm{eff}} = \frac{D}{d_{\mathrm{eff}}}. \tag{10}$$

An argument can be made to use a composite effective modulus that includes the modulus of the transformed martensite, detwinning of the retained martensite and the residual plastic deformation from deformation during fabrication of the spring. Such an approach could be used to account for the drop in actuation force. However, given the behavior observed in [13–15] where the mismatch between dislocations associated with plasticity and the transforming material is mostly accommodated, an approach that computes an effective modulus requires an additional unnecessary step. The effective modulus would require a volumetric determination of the retained martensite and plastic deformation which would again require an assessment of the shear strain. Thus there is merit in an approach that incorporates an effective diameter associated with material in the wire that can undergo a phase transformation based on an assessment of the shear strain.

The shear strain in this analysis approximates the true strain caused by the load aligned with the spring axis. Even though the outer radius of the wire is expected to be plastically deformed, the equations use a linear relationship to accomplish this approximation. This choice was made based on the linear relationships observed and justified in [1] and the transformation occurring in the presence of plastic deformation [13–15]. Ideally, the most accurate method of defining the shear strain would be based on the three-dimensional geometric evolution of the springs as they deform from the loading. This poses practical difficulties and the objective here was to leverage the previously proven approach and characterize the shear strain in a tractable manner while updating the evolving geometry. In the following, we consider a few ways that this can be done and examine the validity of the approach with the acquired data.

The strain in the system can be expected to be linear from the center of the wire, despite the plastic deformation, as it arises from the change in geometry. Furthermore, the polar moment of inertia of the wire can be considered to be constant during loading. The outer radius of the wire is where maximum strain is expected and will not necessarily correspond to maximum stress due to the plastic deformation in this region of the wire. To compensate for this offset, the strain is modeled at where the shear stress is largest but still expected to behave linear elastic, again based on the linear relationships observed and justified in [1]. This is accomplished using the effective wire diameter instead of the nominal wire diameter. This results in the following approximation of the shear strain in the system in Eq. 11.

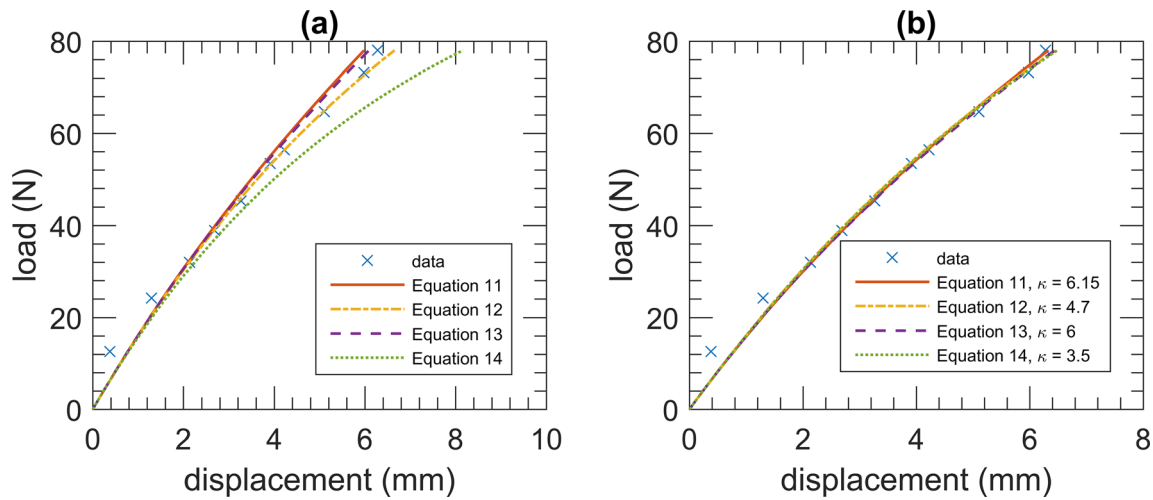$$\epsilon_{\mathrm{r}\theta} \approx \frac{8FDd_{\mathrm{eff}}}{G\pi d_0^4}. \tag{11}$$

Fig. 4 Model comparison for a spring index, C (ratio of spring diameter to wire diameter) of 3.73: **a** loss factor of $\kappa = 5$ from Eq. 9 and predictions using Eqs. 11–14 and **b** predictions from Eqs. 11 to 14 with fits for the loss factor as indicated in the legend

Another approach applies the effective wire diameter in the same manner as Eq. 1. The analytical approach in [1] is based on the strain energy of the system, accounting for the geometric effects of pitch and curvature. Since the model updates the geometry considering the contribution of displacement to strain energy, the approximation for the shear strain can adopt a similar approach. This results in Eq. 12, which attributes the strain entirely to the new geometry of the system.

$$\epsilon_{r\theta} \approx \frac{8FD}{G\pi d_{\text{eff}}^3}. \tag{12}$$

The simplest solution for the approximate strain is to assume that the expected linear behavior of the strain from the center of the wire is completely independent from the change in effective diameter. The approximate strain would then depend only on the load and the changing spring diameter. This results in Eq. 13 which is a conveniently simple function that is nearly linear with the applied loading. This approach assumes that plastic deformation does not change the shear modulus (again consistent with [13–15]). A more rigorous approach would be correct for the plastic modulus, perhaps using an approach outlined in [1] to determine the apparent plastic modulus. However, this improvement is beyond the scope of this paper and is not used here.

$$\epsilon_{r\theta} \approx \frac{8FD}{G\pi d_0^3}. \tag{13}$$

The final approach considered here uses the shear stress equation developed in [10] which takes a more rigorous approach in accounting for the geometric effects of the helical geometry. The equations used by [1] expand on [10] and use truncated equations ignoring higher-order terms.

Using the same reasoning that resulted in Eq. 12 for continuously updating the wire diameter, the shear strain in the system can be represented by Eq. 14 which more accurately represents strain in the system including the effects of curvature from the mean spring diameter. This equation and Eq. 12 behave similarly and may for practical purposes nearly match in effects on the spring displacement. This equation is more complex due to the additional updating term, the spring index, C_{eff}, and may not be necessary considering the accuracy of the model.

$$\epsilon_{r\theta} \approx \frac{8FD}{G\pi d_{\text{eff}}^3}\left(1 + \frac{5}{4C_{\text{eff}}} + \frac{7}{8C_{\text{eff}}^2}\right). \tag{14}$$

The shear strain that best predicts the displacement behavior of the spring and maintains mathematical stability would provide a useful model for the springs and was tested in Fig. 4. To better determine how strain affects the behavior, Fig. 4a compares the various models for the same loss factor ($\kappa = 5$). The similarity between Eqs. 11 and 13 in Fig. 4a is unexpected considering that Eq. 11 has two iterating terms and Eq. 13 has only one iterating term. This may result from the lack of sensitivity to the additional iterating term of the shear strain. The difference between the fully updating geometry of Eq. 14 and the other equations is noticeable indicative of the influence of geometry on the shear strain.

Where Fig. 4a shows the differences between the shear strain, Fig. 4b shows their similarities. The outputs can be quite similar when applying different loss factors to each equation to fit the real data. For practical purposes, this means that any of these equations can be used to predict the spring behavior if the loss factor is kept independent between the different equations. The other practical limitation of these models involved mathematical stability. All

Fig. 5 Acquired load–displacement data of shape memory alloy spring actuators with decreasing spring indices, C (ratios of spring diameter to wire diameter). Symbols are the experimental load–displacement data and the lines are generated from Eqs. 1 to 8 following model refinement with the effective spring index, C_{eff} in Eq. 10
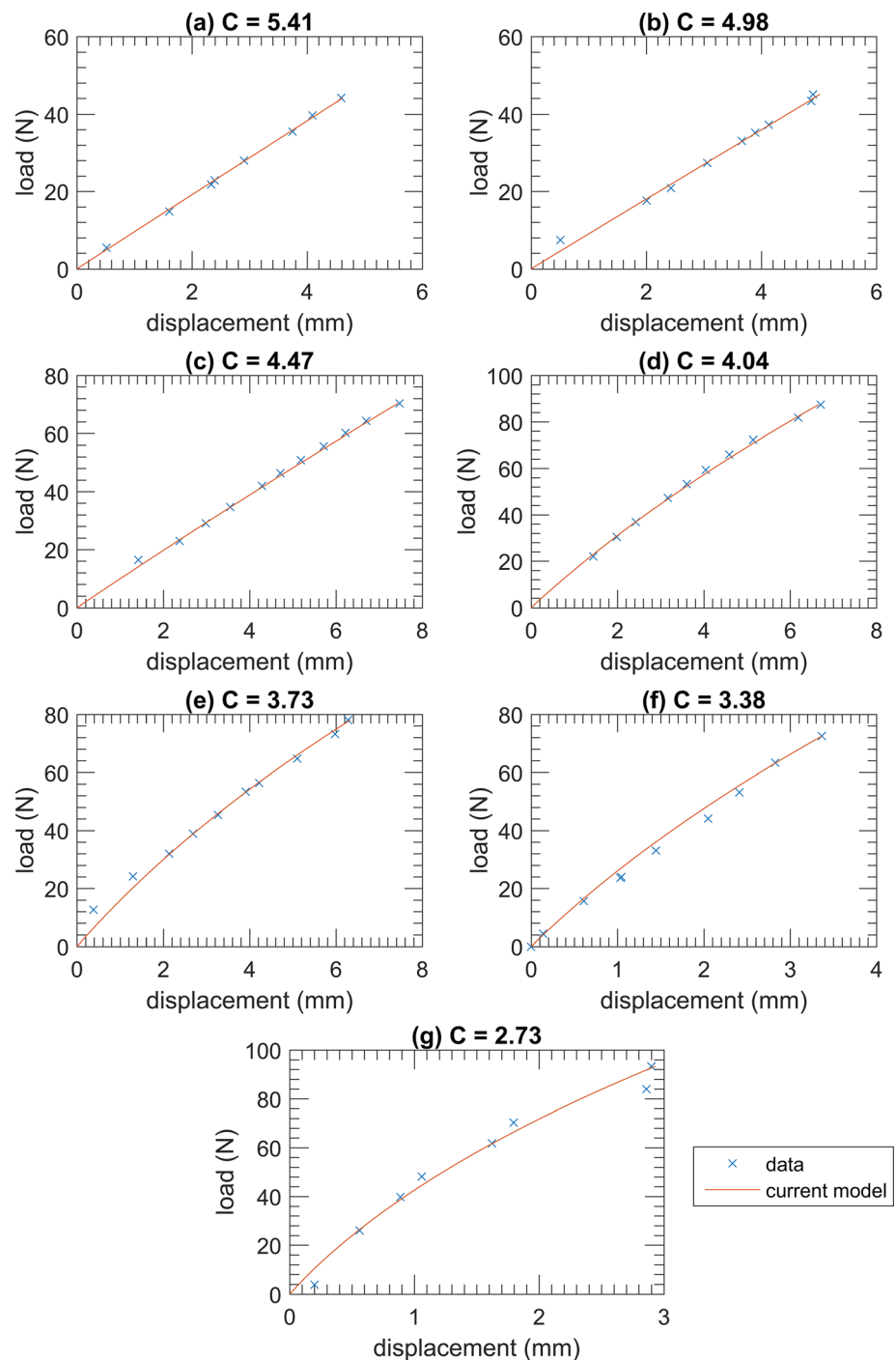
strain models remain stable within any reasonable deflection for the compression springs that were tested. However, if the models are assumed to work with tension springs instead, the deflections can be more than the usable compressive stroke of the spring. Plotting these equations assuming very large deflections show that Eq. 14 based on the strain derived in [10], as well as Eq. 12 that ignores the higher-order terms, begins to exhibit unstable behavior. Equations 11 and 13 remain stable throughout the range

but begin to diverge from each other. An important observation at these deflection scales shows that the unstable equations exhibit cubic behavior well before the instability of the stable models. This behavior may be necessary to explore in future experiments in order to validate one of these models for much larger deflections, or if a model that doesn't attempt to approximate the strain with Hooke's law is necessary to have an applicable model for large spring deflections in tension. With the

Fig. 6 Loss factor (κ in Eq. 9) versus the spring index (C, ratio of spring diameter to wire diameter) for the various load–displacement responses of shape memory alloy spring actuators. The dotted line is a second-order polynomial fit shown in Eq. 15
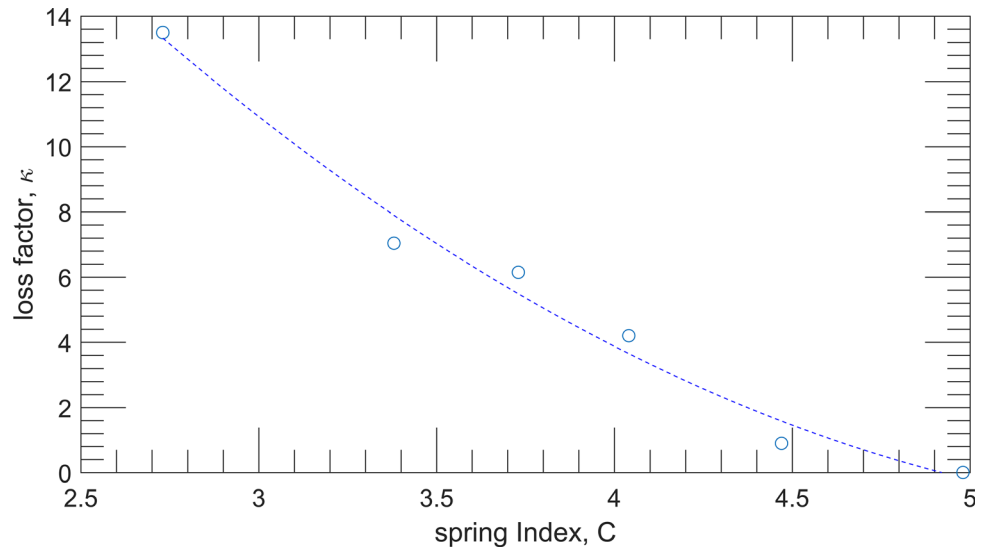
comparisons made between the different strain models and the practical limitations created in these experiments, any of the models developed can adequately describe these springs within the forces and strokes explored. Equation 11 was chosen as the approximate strain model. The model effectively accounts for the plastic deformation as well as maintains mathematical stability at any potential loading.

The method developed for the data in Fig. 4 was applied to experimental data shown in Fig. 3c–g. Equations 9 and 10 were incorporated into Eq. 1, replacing their respective terms, where Eq. 10 completely replaces Eq. 8 as the updating spring index. A unique loss factor was applied to each spring that best matched the actual spring response. The new plots are shown in Fig. 5, with the model refinement showing a much closer agreement to the data when incorporating the effective wire diameter. The previous model fits only at low loadings and would subsequently deviate from the results, as seen in Fig. 3c–g for spring indices of 4 or below. These results indicate an effective practical model for predicting first cycle behavior of shape memory springs manufactured as outlined in the experimental procedures section. Figure 6 collects this data into a plot comparing the loss factor versus the nominal spring index. The trend in Fig. 6 shows a gradual parabolic rise as nominal spring indices decrease. For engineering convenience, a least-squares second-order polynomial was fit to the data resulting in Eq. 15.

$$\kappa \approx 1.48C^2 - 17.4C + 49.8. \qquad (15)$$

We recognize and emphasize that Eq. 15 is merely provided for convenience in designing springs over the entire range of spring indices since data for springs with indices other than those tested in this work may not be readily available. Equation 15 is valid within the range of spring indices of 2.73 to 4.92, above which the loss factor

is 0. This trend may be valid for spring indices below 2.73; however, this is already quite low from a fabrication standpoint. A spring index of 2.00 would be considered the theoretical limit of spring manufacture, below this, the wire would begin to self-intersect. This equation should provide an effective engineering basis to design SMA NiTi springs within a large range that can produce substantial forces compared to their size. However, additional work is needed to determine the range of efficacy of Eq. 15 but a similar model refinement approach can be expected to apply to other SMA alloys. Strain is mostly dependent on the change in geometry and given the ability of the martensitic phase transformation in SMAs to accommodate plastic deformation [12–15], this model could potentially be extended to other SMA alloys.

Conclusions

Shape memory actuators have been introduced into a range of applications, including several that require high forces in restricted spaces. The work of [1] extended [10] and provided an accurate method for modeling the load–displacement behavior of shape memory springs (and therefore the actuation force and stroke) following heating. However, that work failed to accurately predict spring displacement responses for spring indices below 5 as seen from experiments conducted in this work. By accounting for the residual strain induced in the fabrication process, the current model effectively remedies the disparity between data and prediction by decreasing the effective wire diameter under loading. The model is consistent with previously observed phenomena where the phase transformation in plastically deformed SMAs is not significantly altered [12–15]. The proposed model is effective for

springs that have not been fully annealed. An additional annealing process may resolve several of the effects explored in this analysis but may also lead to an unwanted reduction in the strength of the spring and changes in geometry.

The procedures and models outlined in this paper provide an effective toolset for engineers and scientists for predicting shape memory spring actuator response. The model and correction factor applied can be used to implement novel designs that meet increasingly stringent requirements of high force and work densities. This is especially useful in applications where space is a premium. Additional work may be needed to determine the range of efficacy of the fit to the loss factor vs. spring index response determined in this work to other SMAs but a similar model refinement approach can be expected to apply. Strain is mostly dependent on the change in geometry and given the ability of the martensitic phase transformation in SMAs to accommodate plastic deformation, this model could potentially be extended to other SMA alloys. The framework in this work applies to the initial spring actuation cycle but can also be easily extended to predicting the behavior for subsequent cycles as was done in [16, 17]. The approach would be to use the final effective wire diameter after the first few cycles into subsequent cycles, but without incorporating the loss factor in future cycles. From a practical or application point of view, shape memory spring actuators are trained or stabilized for several cycles prior to use. That training or stabilization regimen can easily be integrated in this framework. It is also noted that we did not examine the unloading aspects of the spring actuators in this work. The main objective of the paper was to establish a methodology to accurately predict the actuation force which was being over predicted for shape memory springs with small spring indices. The unloading response, in most actuator applications, usually arises from the actuator being switched off and hence in the more compliant martensitic phase. We nevertheless see no reason why this methodology cannot be applied to unloading of the martensitic phase as was verified in [1, 12, 18, 19]. Lastly, the effective diameter approach presented here has physical basis by examining dislocation densities from spatially resolved transmission electron microscopy experiments, beyond the scope of this present work.

References

1. Nicholson DE, Padula SA II, Noebe RD, Benafan O, Vaidyanathan R (2014) Thermomechanical behavior of NiTiPdPt high temperature shape memory alloy springs. Smart Mater Struct 23(12):13–23
2. Jani JM, Leary M, Subic A, Gibson MA (2014) A review of shape memory alloy research, applications and opportunities. Mater Des 56:1078–1113
3. Calkins FT, Mabe JH, Ruggeri RT (2008) Overview of Boeing's shape memory alloy based morphing aerostructures. Smart Mater Adapt Struct Intell Syst 1:885–895
4. Benafan O, Moholt M (2017) Convergent Aeronautics Solutions Project: Spanwise Adaptive Wing. NASA, Washington, DC
5. Benafan O, Moholt MR, Bass M, Mabe JH, Nicholson DE, Calkins FT (2019) Recent advancements in rotary shape memory alloy actuators for aeronautics. Shape Mem Superelast 5(4):415–428
6. Li C, Ouyang W, Guo H, Tang D, Liu R, Deng Z (2019) Concept and preliminary design of SMA bimetallic strip smart actuator for space adaptive structures. Mater Res Express 6(11):115710
7. Guzik AT, Benafan O (2018) Design and development of CubeSat. In: 44th Aerospace mechanisms symposium, Cleveland
8. Frost M, Sedlák P, Heller L, Kadeřávek L, Šittner P (2018) Experimental and computational study on phase transformations in superelastic NiTi snake-like spring. Smart Mater Struct 27:095005
9. Wheeler R, Benafan O, Calkins FT, Gao X, Ghanbari Z, Hommer G, Lagoudas D, Martin D, Nicholson DE, Petersen A, Phillips FR, Stebner AP, Turner TL (2019) Engineering design tools for shape memory alloy actuators: CASMART collaborative best practices and case studies. J Intell Mater Syst 30(18–19):2808–2830
10. Ancker CJ, Goodier J (1958) Pitch and curvature corrections for helical springs. J Appl Mech 25(4):466–470
11. Padula S II, Qiu S, Gaydosh D, Noebe RD, Bigelow G, Garg A, Vaidyanathan R (2012) Effect of upper-cycle temperature on the load-biased, strain–temperature response of NiTi. Met Trans A 43A:4610
12. Dhakal B, Nicholson DE, Saleeb AF, Padula SA, Vaidyanathan R (2016) Three-dimensional deformation response of a NiTi shape memory helical-coil actuator during thermomechanical cycling: experimentally validated numerical model. Smart Mater Struct 25(9):095056
13. Manchiraju S, Gaydosh D, Benafan O, Noebe R, Vaidyanathan R, Anderson PM (2011) Thermal cycling and isothermal deformation response of polycrystalline NiTi: simulations vs. experiment. Acta Mater 59(13):5238–5249
14. Benafan O, Noebe R, Padula S II, Brown D, Vogel S, Vaidyanathan R (2014) Thermomechanical cycling of a NiTi shape memory alloy-macroscopic response and microstructural evolution. Int J Plast 56:99–118
15. Rathod CR, Clausen B, Bourke MAM, Vaidyanathan R (2006) Neutron diffraction investigation of hysteresis reduction and increase in linearity in the stress–strain response of superelastic NiTi. Appl Phys Lett 88:201919
16. Saleeb AF, Vaidyanathan R (2016) A computationally-efficient, multi-mechanism based framework for the comprehensive modeling of the evolutionary behavior of shape memory alloys. NASA Glenn Research Center, Cleveland
17. Saleeb AF, Padula SA, Kumar A (2011) A multi-axial, multi-mechanism based constitutive model for the comprehensive representation of the evolutionary response of SMAs under general thermomechanical loading conditions. Int J Plast 27(5):655–687

18. Nicholson DE, Padula SA II, Benafan O, Vaidyanathan R (2018) Loading path and control mode effects during thermomechanical cycling of polycrystalline shape memory NiTi. Shape Mem Superelast 4:143

19. Nicholson DE, Padula SA II, Benafan O, Vaidyanathan R (2017) Texture evolution during isothermal, isostrain, and isobaric loading of polycrystalline shape memory NiTi. Appl Phys Lett 110:251903